J. Cent. South Univ. (2020) 27: 2930−2944
DOI: https://doi.org/10.1007/s11771-020-4519-3

Springer

Experimental investigation on failure process and spatio-temporal evolution of rockburst in granite with a prefabricated circular hole

LIU Chong-yan(刘崇岩)[1, 2], ZHAO Guang-ming(赵光明)[1, 2], XU Wen-song(许文松)[1, 2], MENG Xiang-rui(孟祥瑞)[1, 2], HUANG Shun-jie(黄顺杰)[1, 2], ZHOU Jun(周俊)[1, 2], WANG Yun-kun(王云鲲)[3]

1. State Key Laboratory of Mining Response and Disaster Prevention and Control in Deep Coal Mines, Anhui University of Science and Technology, Huainan 232001, China;
2. School of Mining and Safety Engineering, Anhui University of Science and Technology, Huainan 232001, China;
3. Department of Civil & Mineral Engineering, University of Toronto, Ontario, M5S 1A4, Canada

Abstract: To study the mechanism of rockburst and its spatio-temporal evolution criterion, a rockburst simulation experiment was performed on granite specimens, each with a prefabricated circular hole, under different lateral loads. Using micro camera, acoustic emission (AE) system, and infrared thermal imager, the AE characteristics and thermal radiation temperature migration were studied during the rockburst process. Then, the failure mode and damage evolution of the surrounding rock were analyzed. The results demonstrate that increasing the lateral load can first increase and then reduce the bearing capacity of the hole. In this experiment, the hole failure process could be divided into four periods: quiet, particle ejection, stability failure and collapse. Correspondingly, the AE signals evolved from a calm stage, to have intermittent appearance; then, they were continuous with a sudden increase, and finally increased dramatically. The failure of the surrounding rock was mainly tensile failure, while shear failure tended to first increase and then decrease. Meanwhile, damage to the hole increased gradually during the particle ejection period, whereas damage to the rockburst mainly occurred in the stability failure period. The thermal radiation temperature migration exhibited warming in shallow parts, inward expansion, cooling in the shallow parts with free surface heating, inward expansion, a sudden rise in temperature of the rockburst pits, and finally specimen failure. The initial reinforcement support should fully contribute to surface support. Furthermore, an appropriate tensile capacity and good energy absorption capacity should be established in support systems for high-stress roadways.

Key words: rockburst; acoustic emission; spatio-temporal evolution; thermal imaging

Cite this article as: LIU Chong-yan, ZHAO Guang-ming, XU Wen-song, MENG Xiang-rui, HUANG Shun-jie, ZHOU Jun, WANG Yun-kun. Experimental investigation on failure process and spatio-temporal evolution of rockburst in granite with a prefabricated circular hole [J]. Journal of Central South University, 2020, 27(10): 2930−294. DOI: https://doi.org/10.1007/s11771-020-4519-3.

1 Introduction

When a deep high-stress roadway is unloaded after excavation, the engineering environment and rock mass stress state will have changed. Stress redistribution and local concentration can cause cracks and even rockburst of unloaded rock masses

Foundation item: Project(2017YFC0603003) supported by the National Key Research and Development Project of China; Projects(51974009, 51674008) supported by the National Natural Science Foundation of China; Project(201904a07020010) supported by the Key Research and Development Program of Anhui Province, China; Project(2018D187) supported by the Leading Talent Project of Anhui "Special Support Program", Anhui Provincial Academic and Technology Leaders Research Activities Funding, China; Project(gxbjZD2016051) supported by the Excellence Talent Training Program of High School, China; Project (2019CX2008) supported by the Graduate Innovation Fund of Anhui University of Science and Technology, China

Received date: 2020-06-10; **Accepted date:** 2020-08-24

Corresponding author: ZHAO Guang-ming, PhD, Professor; Tel: +86-13955471006; E-mail: guangmingzhao@163.com; ORCID: https://orcid.org/0000-0002-4529-380X

[1−3]. Different from static brittle rock damage, the distinctive feature of rockburst is that rock fragments are ejected at a certain speed and may cause severe damage to personnel and machinery, leading to serious engineering problems [4−6].

Studies have found that most rockbursts occur in hard rock under high stress environments, and that the intensity of a rockburst is closely related to the degree of stress concentration. Furthermore, the initiation pattern and mechanism of rockbursts have been studied by several scholars, and their characteristics have been discussed in different stress situations [7−17]. Thus far, due to the complexity of the rockburst mechanism, the current accuracy of rockburst research is far from meeting the demands of engineering applications. Therefore, the rockburst problem remains a hotspot in rock engineering. If a rockburst simulation experiment was performed with rock specimens of similar geometry and environment to those onsite, the overall structural response and spatial distribution characteristics of the surrounding rock can be simulated more accurately. A sandstone rockburst in four elliptical holes with different axial ratios under biaxial loading was studied as an analogue for underground roadways by WANG et al [18]. Their results indicated that each elliptical hole experienced four main periods: quiet, small particle ejection, spalling, then rockburst. Furthermore, the debris characteristics and the fracture mode of the specimen were analyzed as the axial ratio was increased. LUO et al [19] used a true triaxial test system to investigate red sandstone cube specimens with straight-wall arched holes. The damage process and characteristics of the side walls were analyzed during the test, and the failure mode of the circular hole wall was compared with the test results at the same depth. The tunnel rockburst response characteristics were also studied by HU et al [20] through a prismatic rectangular granite specimen with a hole. The stress−strain characteristics during the test were studied, and microcracks in the fragments were identified using scanning electron microscopy (SEM). Then, the cracking mechanism of the surrounding rock was quantitatively investigated. However, the failure process and mechanism of tunnel rockburst remain unclear, and additional tests with different specimens and loading methods are required.

Acoustic emission (AE) signals are elastic stress waves released when microcracks are generated. They can directly reflect the internal damage of rock mass during its failure evolution, as well as demonstrate the nucleation, development, and expansion of a crack to final failure [21−23]. SU et al [24] conducted impact tests on granite specimens under triaxial loading conditions and analyzed the AE signals during rockburst development. The results indicated that the main AE frequency tended to decrease, while the frequency spectrum distributions were both characterized by low amplitudes, wide frequency bands, and multiple peak shapes prior to the rockburst. ZHANG et al [25] studied the mechanical properties and fracture process of Beishan granite, analyzed the changes in the AE signals and strain energy during rockburst, and divided the rock damage evolution stage according to the AE signals. Their results showed that the strain energy and AE signals had good correspondence under different stress conditions. SUN et al [26] conducted uniaxial compression tests on two rock samples with a tendency to impact. For different types of rocks, the relationship between the mechanical characteristics, AE characteristics, and rockburst were discussed regarding the failure process. In addition, according to the periodic change of the AE cumulative energy curve, combined with the rock failure cusp mutation model, the failure of rock can be predicted to a certain extent. Therefore, AE technology has been one of the best techniques for studying dynamic crack growth and rock failure.

The local stress concentration phenomenon of rock specimens cannot be directly observed. However, the process of rock stress and crack development is generally accompanied by thermal effects. Thermal imaging technology can measure the surface temperature by radiation and has been extensively used in laboratory studies [27]. XIAO et al [28] conducted uniaxial compression tests on natural water coal, natural water-absorbing coal, and saturated coal, and determined the surface damage variables and evolution rules of the coal samples through thermal radiation energy determination. They showed that the occurrence of abnormal infrared points was an important basis for predicting the instability of the coal structure. The

thermal radiation characteristics of a circular tunnel with the stress evolution were studied by WANG et al [29] via a biaxial compression test. When the horizontal load was constant and the vertical load was increased, the heat radiation temperature of the surface changed significantly. This phenomenon verified the evolution consistency of the temperature field and stress field during the excavation of a circular tunnel. Based on fractal, entropy, and statistical theory, the characteristic roughness, entropy, and variance were proposed by LIU et al [30] as indicators to quantitatively describe the evolution characteristics of the infrared radiation temperature field. Many significant achievements have been made concerning infrared thermal imaging and AE technology during the rock failure process, but most studies are based on the surrounding rock unit, and further simulation experiments that consider the spatial and structural characteristics of specimens are required. Furthermore, the method of investigating the spatio-temporal evolution and rupture patterns of rockburst using infrared thermal imaging and AE technology needs to be improved.

In this study, rockburst tests under different lateral loads were conducted on granite specimens each containing a prefabricated hole, and the process was reproduced using micro cameras, AE, and infrared thermal imager monitoring systems. Correspondingly, the AE characteristics and thermal radiation temperature migration were studied, which can provide a scientific basis for revealing the spatio-temporal evolution pattern of tunnel rockburst.

2 Experimental procedures

2.1 Specimen preparation

Granite was selected for the underground rockburst simulation test due to its rockburst tendency. The mineral composition of the granite used was approximately 39.4% quartz, 18.6% potash feldspar, 36.5% plagioclase, 2.1% biotite, and 3.4% of other minerals, and the rock sample was relatively complete and dense. A SEM test was conducted to observe the surface debris and micro cracks (Figure 1(a)). Before the rockburst simulation test, a series of uniaxial compression and Brazilian split tests were performed on a cylindrical specimen with a diameter of 50 mm and a height of 100 mm to obtain the basic physical parameters of the granite (Figure 1(b)) as follows: density of 2.64 g/cm^3, longitudinal wave velocity of 5670 m/s, shear wave velocity of 3541 m/s, porosity of 0.45%, Poisson ratio of 0.27, average uniaxial compressive strength of 220.36 MPa, elastic modulus of 26.8 GPa, and tensile strength of 9.59 MPa. The sample was processed into a cube of 100 mm× 100 mm×100 mm, so that the non-parallelism and non-perpendicularity of the end face should be less than 0.02 mm. Then, a through-hole with a diameter of 30 mm and a depth of 100 mm was drilled in the center of the specimen (Figure 1(c)).

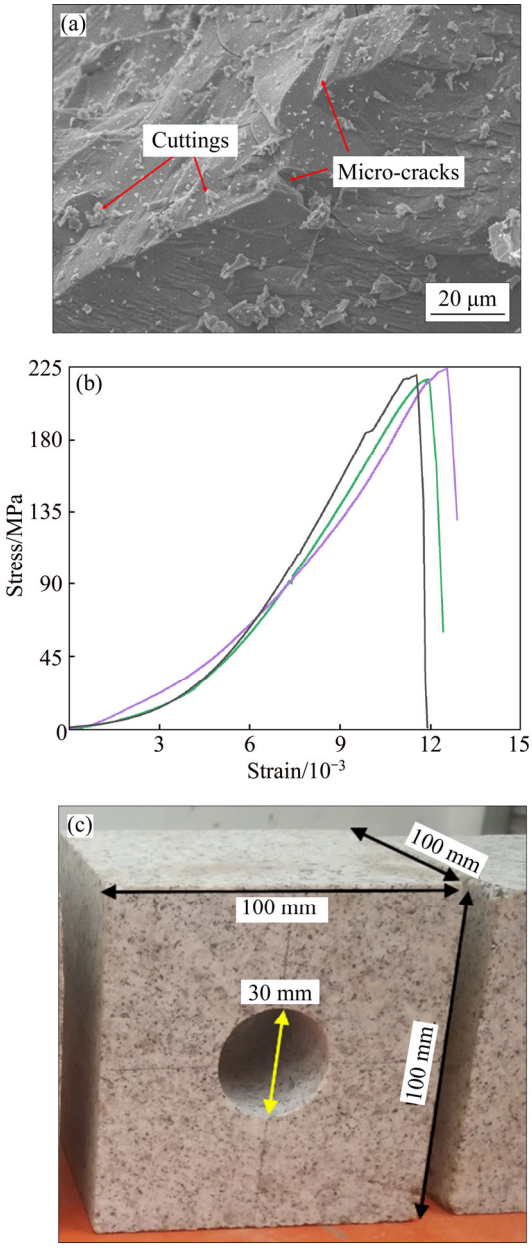

Figure 1 Scanning electron microscopy image of granite fragments (a), uniaxial compressive strength of granite specimen (b), and picture of granite specimen (c)

2.2 Testing system and experimental scheme

The true-triaxial disturbance unloading test system could be independently controlled in three directions in this study. The vertical load was up to 5×10^3 kN and the horizontal load was up to 3×10^3 kN. The loading process was controlled by a digital servo controller, which can carry out single-, double-, and three-axis tests. A self-made microporous camera was adopted to monitor and record the failure situation inside the hole. The MISSCNR600 infrared thermal imaging system was selected for the infrared test. The wave band was tested at 7−14 μm, and the thermal sensitivity was 0.06 °C. When the temperature was 30 °C, the minimum focal length was 0.3 m, and the image frequency was 25 Hz. The Softland DS5 AE system was selected for the AE signal monitoring, and six AE probes were applied to collect the signals. To minimize the impact of noise, the threshold value was set at 40 dB, and the AE sampling frequency was set at 1 kHz−1 MHz. The AE signals could be recorded in real time and three-dimensional positioning information was acquired. Moreover, the sound velocity of the rock specimens was measured by a lead-breaking test.

The temperature of the specimen should be consistent with the surrounding environment before the simulation test. In addition, the loading and monitoring devices should be started simultaneously to ensure consistent time records. Therefore, the response characteristics of the specimen from microcracks to the macroscopic failure can be effectively captured. A diagram of test device installation is shown in Figure 2.

The stress state of the surface surrounding the rock was changed from triaxial to approximately uniaxial or biaxial stress in the excavation process, which resulted in stress readjustment and local concentration. When the concentration of tangential

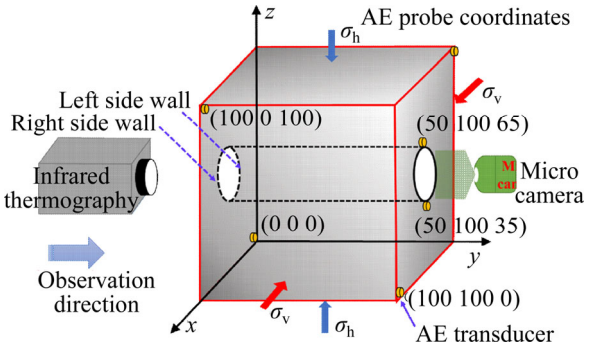

Figure 2 Test device installation diagram

stress exceeds the rock strength, the strain energy will be released violently and cause a rockburst. Thus, this experiment chose the biaxial pressure mode to simulate rockburst. For simulating the tangential stress concentration, the vertical load σ_h was continuously increased while the lateral load σ_v remained stable. In this paper, six groups of loading tests were performed with lateral loads of 5, 10, 15, 20, 25 and 30 MPa, respectively. The test adopted load control and the loading rate was 0.1 MPa/s. From the specific loading stress path, σ_h and σ_v started loading simultaneously to the specified stress value, then σ_v remained constant until the specimen experienced failure.

3 Experimental results

3.1 Stress−strain characteristics

The strength and deformation characteristics of the specimen were different under different stress conditions. Figure 3 shows the stress−strain curve of the granite with holes under different lateral loads. The curve did not drop before the stress peaked, and maintained a good linear characteristic, clearly indicating the brittle failure characteristics of the granite specimen. Furthermore, from the relationship between strain and stress, when the σ_v values were 5, 10, 15, 20, 25 and 30 MPa, the lateral peak strains of granite were calculated as -2.8×10^{-3}, -3.1×10^{-3}, -3.2×10^{-3}, -4.3×10^{-3}, -4×10^{-3} and -1.6×10^{-3}, respectively. As a result, when the horizontal stress remained constant, axial compression occurred due to the continuous increasing of the vertical load, but the rock expanded laterally, and the expansion rate increased as the vertical stress increased. Additionally, the lateral peak strain displayed the trend of first increasing and then decreasing as σ_v increased, and a larger lateral peak strain corresponded to a higher peak strength within a certain range. After the lateral load exceeded 20 MPa, the lateral expansion was limited, so the consumption of elastic energy was reduced, as granite is more likely to be destroyed when the energy is concentrated.

For σ_v values of 5, 10, 15, 20, 25, and 30 MPa, the peak strengths (σ_h) of the granite were 155.45, 166.62, 179.63, 206.69, 190.28 and 165.77 MPa, respectively. It is clear that the peak strengths of the rock mass first increased and then decreased as σ_v

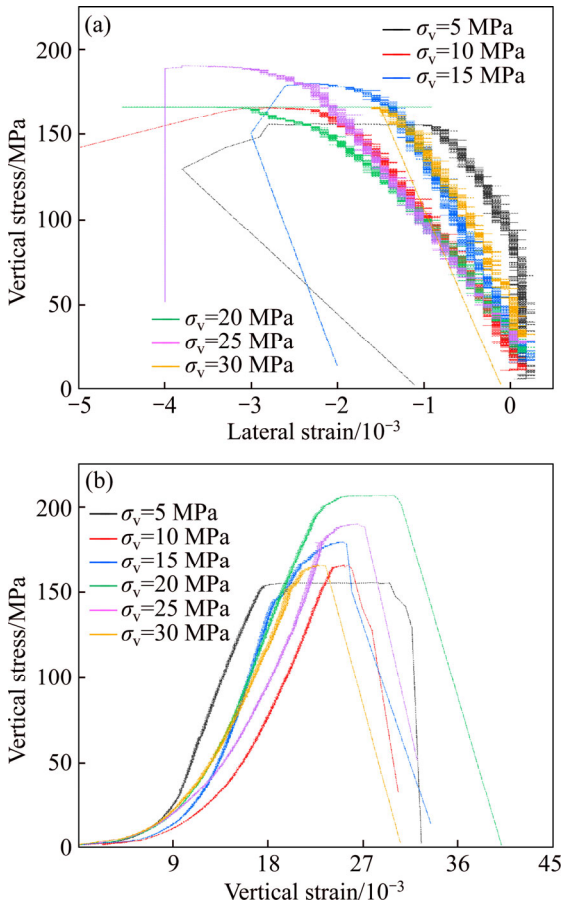

Figure 3 Stress−strain curves under different lateral pressures

increased. This phenomenon is similar to the result obtained by DU et al [31]. With the lateral load promoted, the vertical peak strains of the failure specimens were 15.4×10^{-3}, 18.9×10^{-3}, 19.2×10^{-3}, 25.2×10^{-3}, 22×10^{-3} and 18.2×10^{-3}, respectively. Here, there is also the trend of first increasing and then decreasing, and the bearing capacity and deformation capacity of the granite reached maximum when the lateral load was 20 MPa. Specifically, the lateral pressure affected the load-bearing capacity of the specimen to a certain extent, first strengthening and then weakening under such loading conditions. Therefore, when the stress was concentrated in a certain range, the lateral load strengthened the bearing capacity of the hole and reduced the risk of rockburst. Nonetheless, when the lateral load was higher than the critical value, the stress level was higher and the lateral expansion capacity was lower, which reduces the stability of the hole. When more elastic strain energy is released, the rockburst will be more violent.

3.2 Failure process of specimen

The micro camera and loading system were used to record the entire rockburst process, from particle ejection to collapse of the hole. The specimen with the lateral load of 10 MPa was used as an example to analyze the evolution of rockburst, as shown in Figure 4.

In the simulation test, the hole failure process could be divided into periods of quiet, particle ejection, stability failure, and collapse. During the long period of initial loading, the hole wall was stable. When the vertical load reached 62.11 MPa, small particle ejections started to occur intermittently; thus, the particle ejection period began. At this stage, the stress concentration was low, the size of the particles was small, and the velocity of ejection particles was slow. When the vertical loading reached 89.31 MPa, a small rock sheet ejection occurred in the right wall, and no obvious crack appeared in the hole surface. The direction of the small rock sheet ejection was random and its velocity differed. When the vertical load reached 131.05 MPa, the stability failure period developed. The right local rock plate of area one was bent outward and broken into two rock sheets, from which small particles were ejected. Then, when the vertical load increased to 140.25 MPa, the fractured lower rock sheet suddenly lost its stability and slipped down. Meanwhile, the rock plate of area two was also bent outward and broken into two rock sheets. Subsequently, the right surrounding rock was destroyed along the axial buckling plate, and the surface of the circular hole was flaked off and accompanied by continuous pellet ejection. Consequently, a “V”-shaped pit was gradually formed, and the left wall began to show small area failure.

When the vertical stress reached 152.26 MPa, particles and rock sheets were continuously ejected from the middle of the V-shaped pit on the right side of the cave wall, which enlarged the width and depth of the V-shaped pit, accompanied by noise and a large amount of fog-like dust. Simultaneously, the failure area on the left was partially connected and continued to develop. When the vertical load increased to 163.40 MPa, the fractured rock plate of the right wall was completely spalled, debris with different particle sizes continued to appear, and the failure area of the left wall was completely transited

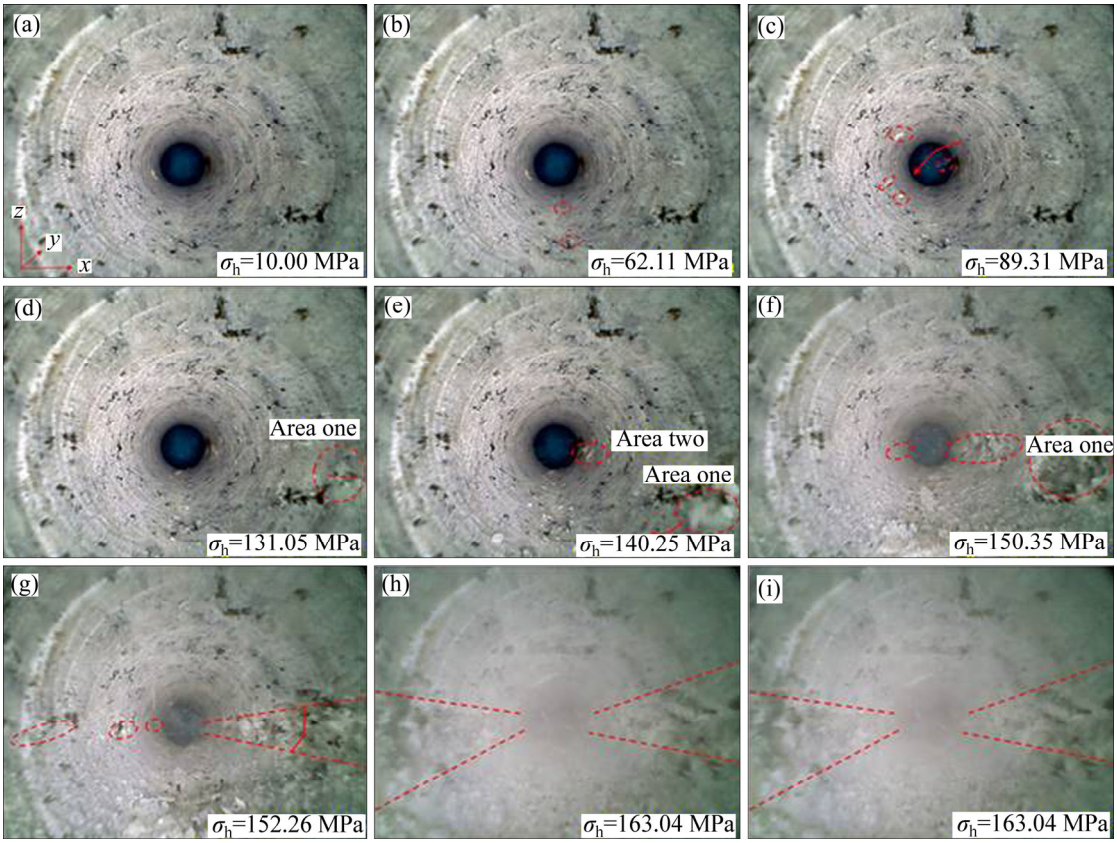

Figure 4 Hole failure process recorded using micro camera

along the axial direction. When the vertical load was 165.04 MPa, the V-shaped pit began to deform under the compression as it entered the collapse period. Finally, the specimen experienced failure.

3.3 Spatio-temporal evolution characteristics of hole failure process

With the development and expansion of rock cracks under the load, energy will be released in the form of elastic wave, which can be received by the AE probe. The location of the rupture can be retrieved by the arrival time of the P wave. To reflect the evolution characteristics of a rockburst, the inversion results were screened, and the locating point near the hole was identified. The AE values differed under different lateral pressure conditions, but the change trend remained similar. The specimen with σ_v=15 MPa was analyzed as an example.

The spatio-temporal evolution can also be divided into four periods, as shown in Figures 5 and 6. Before the vertical load reached 66.41 MPa, the stress concentration area was small, the original cracks first appeared and then closed, and the rockburst remained in the quiet period.

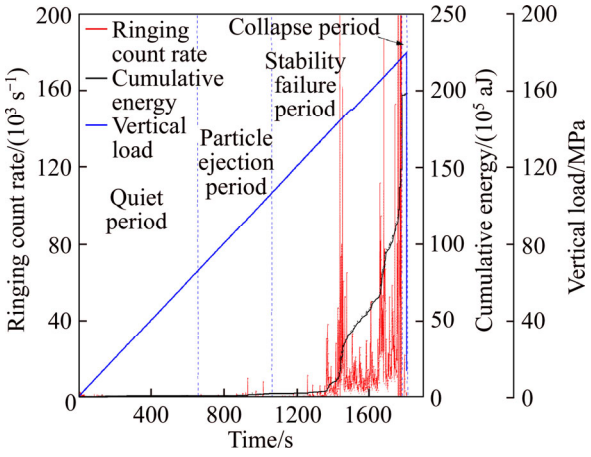

Figure 5 Relationship between the acoustic emission (AE) ringing count, cumulative energy, stress, and time

Correspondingly, there was no apparent damage to the hole wall, the AE signal was relatively weak, the ring count rate was maintained at a low value, the cumulative energy value was low in magnitude, and the locating points were randomly distributed near the surface of the hole, indicating that the quiet period was generally a period of energy accumulation.

After the vertical load exceeded 66.41 MPa, the surrounding rock cracks continued to develop,

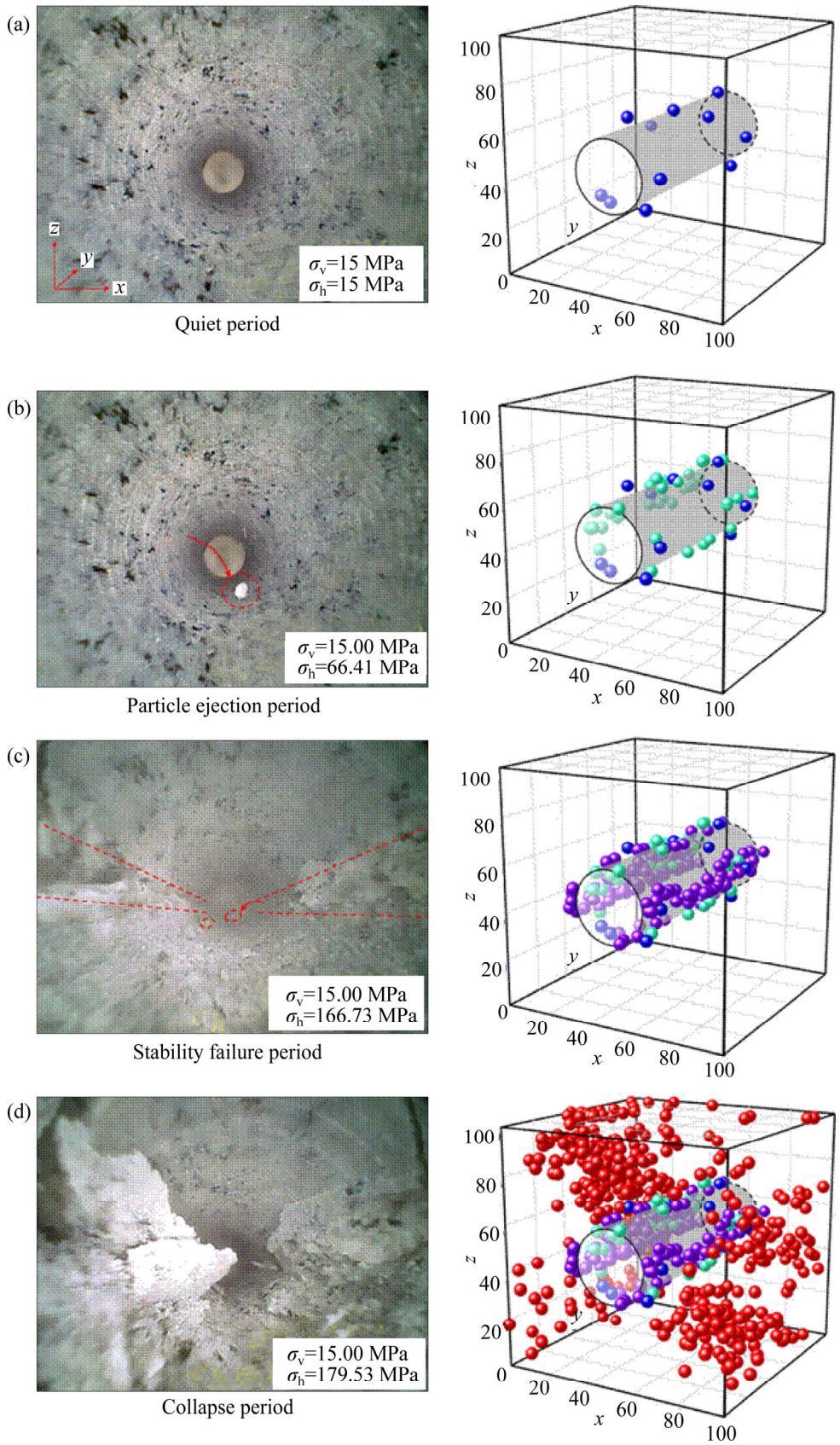

Figure 6 Images of hole rockburst corresponding to AE spatio-temporal evolution at different periods (Blue, cyan, and purple represent the locating points generated near the hole during the quiet period, the particle ejection period, and the stability failure period, respectively. The clustered state of the red locating points depicts the shear shape after overall failure)

and small particle ejection occurred in the hole, but the surrounding rock did not exhibit obvious bending deformation. Correspondingly, the AE energy rate and cumulative energy started to rise abruptly, and the AE signal was not displayed continuously. The ejection of small particles caused a slight release of energy during the rockburst process, but more energy continued to accumulate simultaneously. In addition, the number of locating points increased, caused by the particle ejection. Moreover, it gradually expanded inward from the hole surface and formed a local concentration area on the left side of the hole. Further, under the action of tangential stress, cracks in the hole continued to nucleate and expand, and cracks near the surface formed blocks or rock sheets, so particle ejection occurred in the hole wall.

After the vertical load exceeded 107.01 MPa, the rockburst remained in the stability failure period, local rockburst began in the hole, the hole bent locally and the rock slab broke off with continuous pellet ejection, the failure depth increased, and two rockburst bands gradually formed. Correspondingly, there were continuous AE signals at this stage, and the ring count rate increased suddenly many times, showing a multi-peak state, accompanied by a stepwise increase in cumulative energy. At the peak point of the ring count rate, the rock cracks developed and formed a local rockburst, usually with a small amplitude signal oscillation between the two peaks, and the slope of the cumulative energy curve slightly decreased, reflecting that there was a gradual process of energy release-storage-release between the two rockburst bands. In addition, the locating points began to expand along the concentration points on the left wall. As σ_h continuously increased, the locating points on both sides significantly increased, while the range gradually increased and developed deeper into the surrounding rock. Then, two obvious concentrated bands formed, corresponding to the V-shaped pit. The rockburst led to a large release of elastic strain energy which accumulated during the stability failure period, and the bearing capacity of the roadway was weakened due to the continuous destruction of the surrounding rock.

This study found that when the vertical load was 176.70 MPa, the ring count rate experienced a short calm period, the rockburst activity weakened, and then the hole wall gradually deformed until it collapsed. During the collapse period, the ring counting rate and cumulative energy slightly increased again. Most of the locating points appeared far away from the tunnel wall and gradually formed an “X”-type shear fracture surface. The concentrated area of locating points was basically consistent with the final principal fracture surface of the model. Furthermore, it was found that a small quiet period, after the formation of the V-shaped rockburst pit, can be used as the precursor signal of hole collapse.

4 Discussion

4.1 Acoustic emission signals of cracking mechanism

The characteristics of an AE waveform are generally regarded as an effective way to reflect the fracture failure mode. Previous studies have demonstrated that the RA value and average frequency (AF) can reflect the crack type inside a material structure; RA is the ratio of the rise time and amplitude, and the AF is obtained from the ratio of the ring count and duration. Generally, AE signals with low AF and high RA values usually represent the generation or development of shear cracks. On the contrary, high AF and low RA values represent the generation of tensile cracks [32]. The density distribution of the AE, RA and AF values are shown in Figure 7. The red area represents the density core area, while the blue area density is equal to zero, indicating no data distribution, and the transition from the red to blue area represents a certain amount of data.

It was found that as the lateral load increased, the total number of data points first increased and then decreased. The variation of the core density area followed the same trend. Furthermore, the AF was widely distributed across the longitudinal axis, while the maximum value of RA first increased and then decreased as the lateral load was increased. From the above analysis, it can be seen that the data were scarce and scattered in high RA and low AF intervals. On the contrary, the data were relatively dense in the high AF and low RA intervals, indicating that the cracks, produced under different lateral loads, were all tension shear composite cracks, particularly tension cracks, which is consistent with the previous research results obtained by HU et al [20]. Furthermore, the

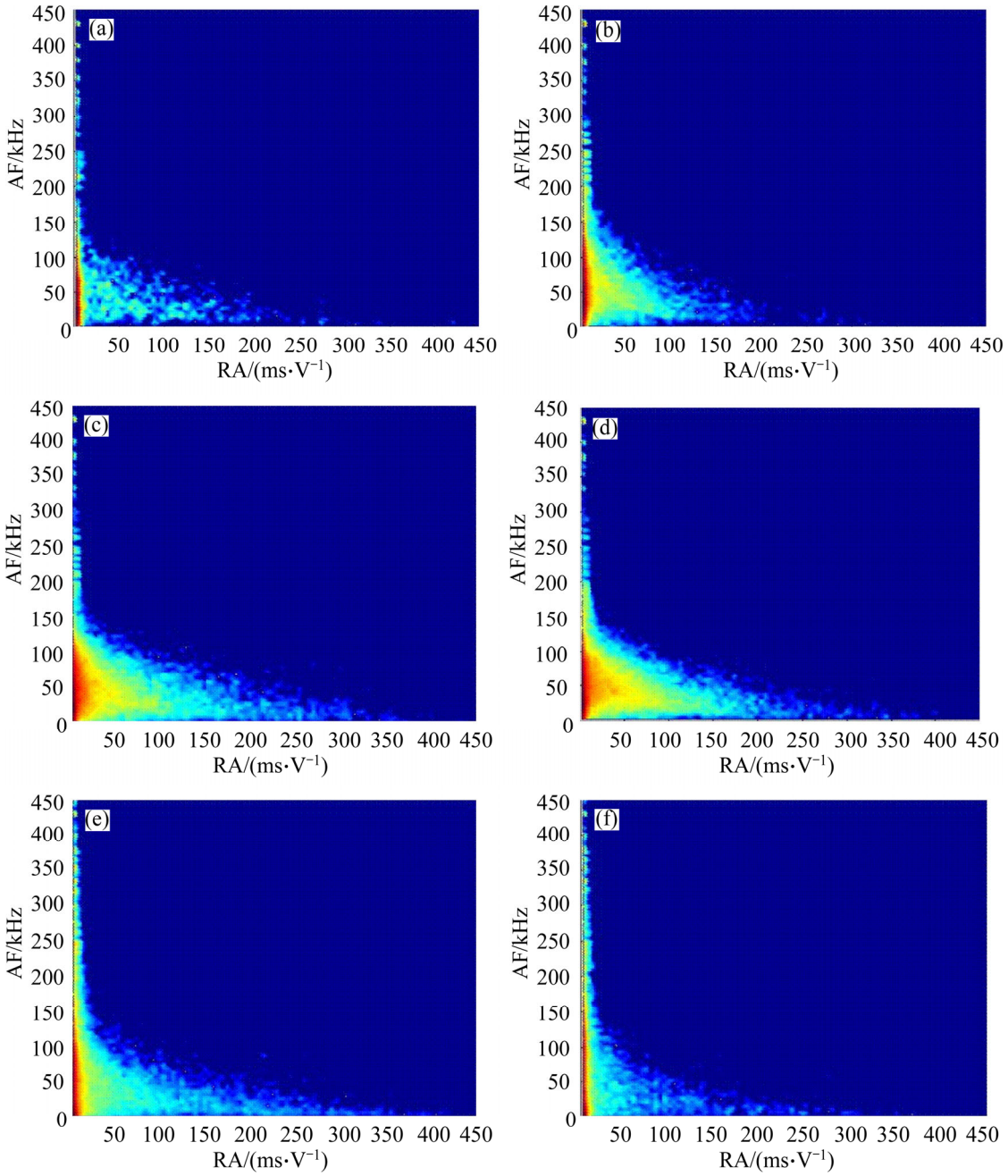

Figure 7 Density distribution map of AE RA-AF: (a) σ_v=5 MPa; (b) σ_v=10 MPa; (c) σ_v=15 MPa; (d) σ_v=20 MPa; (e) σ_v=25 MPa; (f) σ_v=30 MPa

tangential stress on the hole continued to increase during the test. According to the Griffith strength theory, the stress concentration phenomenon was more likely to occur near the tip of the tensile crack and promoted the expansion of the cracks. Thus, the failure of the surrounding rock mainly involved a gradual increase of tensile stress caused by compression.

As the lateral load increased, the number of shear cracks first increased and then decreased. In addition, the peak strength of the surrounding rock first increased and then decreased, which has the same evolution trend as that of the shear cracks. In most cases, regarding the bonding strength, between the sample mineral particles, it was generally accepted that the shear strength was greater than the tensile strength. More specifically, the bonding mineral was generally resistant to shear stress and not tensile stress, and the shear cracks directly affected the peak strength. Therefore, when the lateral load was 20 MPa, the vertical load value and shear cracks reached maximum simultaneously.

From the rockburst process and the rock failure mode, it can be inferred that the formation of the rockburst pits progressed as shown in Figure 8. As the vertical stress continued to increase, the local rockburst developed from initial micro-cracks to particle ejection, and there was no obvious buckling deformation in the rock specimens (Figure 8(a)). The increased tangential stress promoted the expansion of new tensile cracks, and parallel cracks were generated by tension stress near the wall. Then, the surrounding rock was divided into blocks or sheets (Figure 8(b)). Meanwhile, it can be approximately considered that the confining pressure was reduced and the stress state was similar to uniaxial compression. When the stress concentration reached a certain value, the rock slab buckled and failed. Subsequently, rockburst occurred (Figure 8(c)). Afterward, the failure behaviors progressed to a deeper area, and debris ejection was accompanied by the spray mist of particles. Eventually, a V-shaped pit was formed (Figure 8(d)).

4.2 Thermal radiation characteristics of surrounding rock failure

Rock mass is an engineering material with natural micro-defects. The damage of surrounding rock is caused by the continuous evolution and expansion of a large number of randomly distributed cracks and fractures. The variation of AE energy corresponds to the development of these rock cracks [28]. To study the evolution of rockburst damage, the damage variable D was calculated by the ratio of n (AE cumulative energy) to N (AE total energy). Then, a relation diagram between the damage and stress was drawn (Figure 9), and the damage process was divided into four stages corresponding to the failure process of the surrounding rock.

$$D=\frac{n}{N} \tag{1}$$

The obtained infrared thermal image was denoised by an image difference algorithm, and the spatial evolution characteristic of the thermal radiation temperature field was analyzed.

$$g_k(x,y)=f_k(x,y)-f_1(x,y) \tag{2}$$

where k is the index of the infrared thermal image sequence; $f_k(x,y)$ and $f_1(x,y)$ are the matrices comprising the temperature values of each pixel extracted from the kth and the first thermal image, respectively; $g_k(x,y)$ represents the difference matrix between each thermal image and the first thermal image.

On the right side of the hole, a square with a length of 10 mm was used for the analysis and was applied to study the thermal imaging temperature migration characteristics, as well as the D characteristics, during the rockburst.

The thermal imaging data and damage variables of the σ_v=25 MPa specimen were studied. Before the vertical pressure reached 82.49 MPa, the damage variable D hardly increased, and the amount of damage to the hole was only 1.18%. The stress concentration did not appear in the hole surface, and the surface temperature manifested an overall low temperature state, as shown in Figure 9(a).

The damage gradually accumulated during the particle ejection period, and the curve of the damage variable D began to increase at a lower

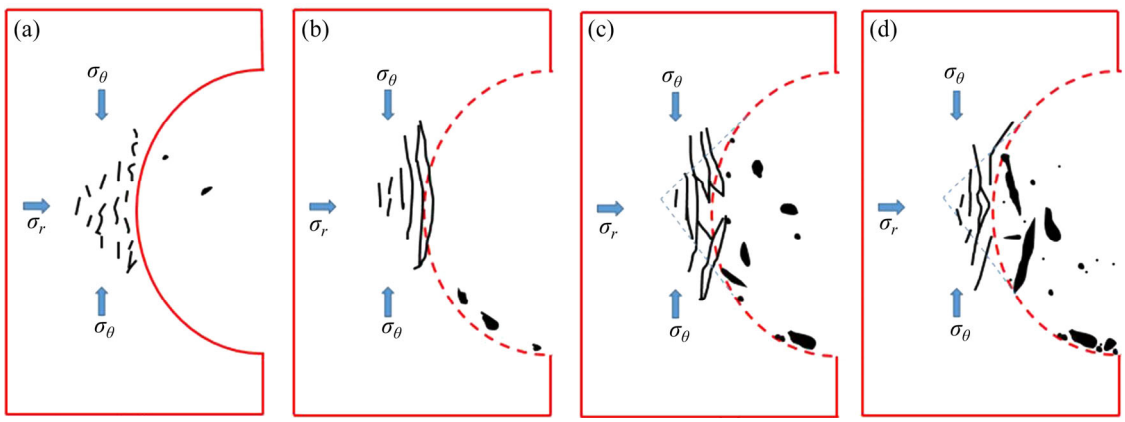

Figure 8 Schematics of failure process for individual local rockbursts: (a) Particle ejection period; (b) Splitting into thin sheets; (c) Buckling failure; (d) Fragment ejection

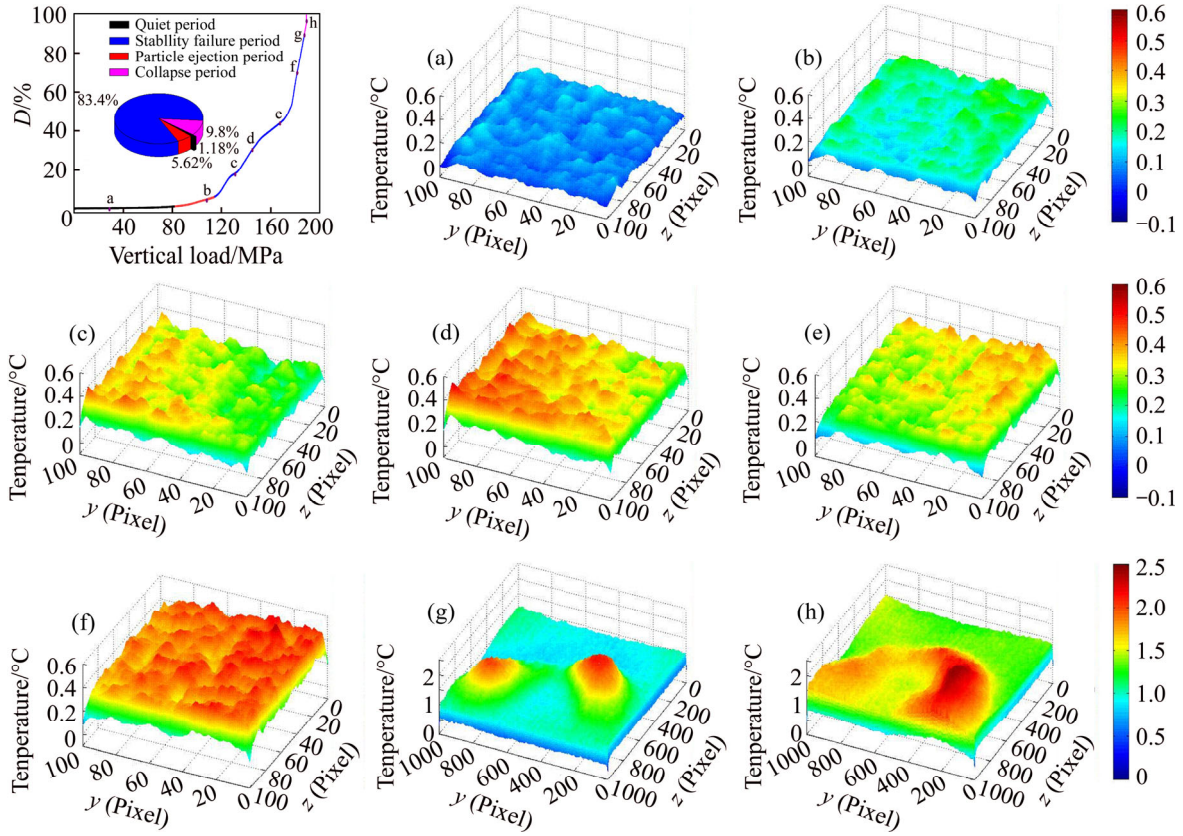

Figure 9 Thermal imaging migration and curve of damage variable D: (a–h) correspond to points (a–h) in curve of D and vertical load

slope. At this stage, the amount of surrounding rock damage was 5.62%, caused by the particle ejection. As shown in Figure 9(b), the concentration of heat occurred as the load increased. In addition, some low temperature points appeared near the hole wall caused by the ejected small particles.

After the rockburst entered the period of stability failure when the vertical load was 115.06 MPa, the curve of the damage variable D changed from a nonlinear growth to a steep increase, and the cumulative damage reached 83.4%. Meanwhile, the heat-concentrated area became increasingly obvious, mainly appearing in the shallow part of the specimen and exhibiting a decreasing trend of waveform inward. Additionally, the surrounding rock damage variable D reached 20%, as shown in Figure 9(c). Due to the rise of tangential stress, the surrounding rock was stretched and induced plate splitting. Then, the thermal elastic effect developed as a result of the volume expansion [33]. Consequently, the inter-slate temperature decreased slightly with high-temperature-embedded low-temperature bands, and D reached 30%, as shown in Figure 9(d). Moreover, the buckling and rupture of the rock plate was accompanied by particle ejection on the hole surface. Since this time, the temperature of the surface decreased relatively, and the stress concentration transferred to the free surface. Simultaneously, the temperature of the new free surface increased accordingly. Therefore, the temperature of the shallow part of the surrounding rock decreased, and the high temperature area migrated to the deep part, as shown in Figure 9(e). When rockburst occurred, the specimen released a large amount of energy. This then generated a fracture, friction, and a particle jet in the deep rock plate of the rockburst pit, and the thermal imager showed a high temperature state. The temperature of the deep rockburst pit was higher than that of the shallow pit, and D reached 67%, as shown in Figure 9(f).

When the vertical load reached 188.28 MPa, D reached 89.41% by rockburst. Afterward, the damage entered the collapse period, the D curve had a large rising slope, and a small change in stress would cause great damage to the specimen. In the collapse period, the specimen was squeezed and

deformed significantly before hole collapse, and a large amount of friction was generated. Furthermore, the temperature rapidly increased and the temperature difference varied greatly. The overall thermal image expressing this is shown in Figure 9(g). Subsequently, the V-shaped high-temperature shear zone formed when the rock specimen was destroyed (Figure 9(h)).

4.3 Reflections on rockburst control

The brittleness characteristics of the surrounding rock determined the range of rupture and potential damage zone, and the increase of the lateral load contributed to first strengthening and then weakening the bearing capacity of the surrounding rock. Therefore, projects must consider the influence of lateral load on the failure mode of surrounding rock, and that the transformation of the failure mode can improve the bearing capacity of surrounding rock. Furthermore, violent rockburst failure began when the tensile fracture occurred. Therefore, when support patterns are designed, the tensile strength of the bearing body should be enhanced with good transformation ability.

In the shallow surrounding rock close to the excavation face, the confining pressure level was low, and the tangential stress concentration level was high, indicating an increased risk of rockburst. However, particle ejection evolved into rock flaking during the local rockburst, and the damage scale of the shallow surrounding rock was weak. Moreover, when controlling the development of cracks and maintaining the stability of small crack areas, special attention should be paid to the initial reinforcement of the surface support, and the penetration and deformation of cracks should be controlled.

The V-shaped pit gradually formed from the outside to the inside by the step expansion failure, and each violent rockburst was caused by stress concentration. Thus, the support pattern can effectively limit the fracture propagation and improve the shear strength of rock mass. Moreover, the support pattern maintained the ability to resist rockburst impact or absorb energy. More specifically, if the stiffness of the supporting system was insufficiently large and the support pattern did not deform well enough to absorb energy under the action of shockwaves, it was not only easy to induce rockburst with greater energy, but also possible to cause the failure of the support system near the failure zone.

The stress concentration area can be identified by the heat radiation temperature, and the temperature warning value can be set according to specific conditions of the surrounding rock. When the temperature of the surrounding rock shallow part increased and spread inward, the damage reached approximately 30% or higher. At this time, the construction behaviors should be stopped to avoid secondary disturbance to the stress concentration area. In addition, pressure relief measures and reinforcement support should be established on the surrounding rock to prevent the occurrence of severe rockburst.

5 Conclusions

In this paper, the true-triaxial disturbance unloading rock testing system is introduced to perform rockburst simulation experiments, and the rockburst process was studied via an AE monitoring system and infrared thermal imager. The spatio-temporal evolution characteristic of rockburst is preliminarily revealed and the main conclusions are as follows:

1) When $\sigma_v \leq 20$ MPa, the increased lateral load will promote the deformation and bearing capacity of a granite specimen. When $\sigma_v > 20$ MPa, the lateral load limits rock deformation and weakens its bearing capacity.

2) In the quiet period, rockburst was constantly generated and the AE signals were weak. Then, when the stress gradually concentrated, particle ejection occurred in the surrounding rock, and AE signals appeared intermittently. Meanwhile, the energy rate and accumulated energy rose slightly, and the locating points were locally concentrated. During the period of stability failure, the surrounding rock buckled and deformed, flaking of the rock was accompanied by violent particle ejection, and the failure continued to deepen. Correspondingly, the ring count rate and energy increased abruptly many times, and the locating points expanded axially, forming two obvious bands. When the V-shaped rockburst pit formed, the ring count rate had a short period of calm accompanied by weakened rockburst activity. Ultimately, the rock blocks folded inward in the vicinity of the rockburst zone, then the hole

collapsed, and the concentrated area of the locating points basically coincided with the fracture surface, forming an X-type conjugate shear fracture zone.

3) With the increase of the lateral load, the core density area of the RA-AF map grew first, and then decreased. The surrounding rock mainly experienced tensile failure. Whereas, the shear failure behaviors first increased and then decreased. Moreover, the influence of lateral load on the failure mode of the surrounding rock was found to be directly related to the rock peak strength.

4) Eighty percent of the damage area appeared in the period of stability failure. As the stress level increased, the heat radiation temperature became higher. First, this phenomenon was concentrated in the shallow part of the surrounding rock and gradually expanded into the internal surrounding rock, forming a low-temperature nest in the high temperature area. When the surrounding rock buckled and failed, the high temperature zone shifted to a new free surface, gradually increased, and expanded again.

5) In the support design of a high-stress roadway, the surface support should make full use of initial reinforcement. In addition, an appropriate tensile capacity and good energy absorption capacity should also be considered in the support system. Furthermore, the degree of stress concentration and transformation can be identified through a thermal radiation system, and pressure relief measures and reinforcement support should be established in time to prevent severe rockburst.

Contributors

The overarching research goals were developed by LIU Chong-yan, ZHAO Guang-ming and XU Wen-song. LIU Chong-yan, HUANG Shun-jie and ZHOU Jun provided the experimental methods and data, and analyzed the experimental data. The initial draft of the manuscript was written by LIU Chong-yan and ZHAO Guang-ming, MENG Xiang-rui, WANG Yun-kun revised and reviewed the manuscript. All authors replied to reviewers' comments and revised the final version.

Conflict of interest

LIU Chong-yan, ZHAO Guang-ming, XU Wen-song, MENG Xiang-rui, HUANG Shun-jie, ZHOU Jun, and WANG Yun-kun declare that they have no conflict of interest.

References

[1] SI Xue-feng, GONG Feng-qiang. Strength-weakening effect and shear-tension failure mode transformation mechanism of rockburst for fine-grained granite under triaxial unloading compression [J]. International Journal of Rock Mechanics and Mining Sciences, 2020, 131: 104347. DOI: 10.1016/j.ijrmms.2020.104347.

[2] SIREN T, KANTIA P, RINNE M. Considerations and observations of stress-induced and construction-induced excavation damage zone in crystalline rock [J]. International Journal of Rock Mechanics and Mining Sciences, 2015, 73: 165−174. DOI: 10.1016/j.ijrmms.2014.11.001.

[3] LABIOUSE V, VIETOR T. Laboratory and in situ simulation tests of the excavation damaged zone around galleries in opalinus clay [J]. Rock Mechanics and Rock Engineering, 2014, 47: 57−70. DOI: 10.1007/s00603-013-0389-4.

[4] ZHANG Chuan-qing, FENG Xia-ting, ZHOU Hui, QIU Shi-li, WU Wen-ping. Case histories of four extremely intense rockbursts in deep tunnels [J]. Rock Mechanics and Rock Engineering, 2012, 45(3): 275−288. DOI: 10.1007/s00603-011-0218-6.

[5] ZHOU Xiao-ping, PENG Sen-lin, ZHANG Jian-zhi, QIAN Qi-hu, LU Ri-chao. Predictive acoustical behavior of rockburst phenomena in Gaoligongshan tunnel, Dulong river highway, China [J]. Engineering Geology, 2018, 247: 117−128. DOI: 10.1016/j.enggeo.2018.10.023.

[6] LIU Fei, TANG Chun-an, MA Tian-hui, TANG Lie-xian. Characterizing rockbursts along a structural plane in a tunnel of the Hanjiang-to-Weihe river diversion project by microseismic monitoring [J]. Rock Mechanics and Rock Engineering, 2018, 52(6): 1835−1856. DOI: 10.1007/s00603-018-1649-0.

[7] LUO Yong, GONG Feng-qiang, LI Xi-bing, WANG Shan-yong. Experimental simulation investigation of influence of depth on spalling characteristics in circular hard rock tunnel [J]. Journal of Central South University, 2020, 27(3): 891−910. DOI: 10.1007/s11771-020-4339-5.

[8] FENG Xia-Ting, LIU Jian-po, CHEN Bing-rui, XIAO Ya-xun, FENG Guang-liang, ZHANG Feng-peng. Monitoring, warning, and control of rockburst in deep metal mines [J]. Engineering, 2017, 3(4): 538−545. DOI: 10.1016/J.ENG.2017.04.013.

[9] JIANG Bang-you, GU Shi-tan, WANG Lian-guo, ZHANG Guang-chao, LI Wen-shuai. Strainburst process of marble in tunnel-excavation-induced stress path considering intermediate principal stress [J]. Journal of Central South University, 2019, 26(4): 984−999. DOI: 10.1007/s00603-018-1649-0.

[10] ZHOU Jian, LI Xi-bing, SHI Xiu-zhi. Long-term prediction model of rockburst in underground openings using heuristic algorithms and support vector machines [J]. Safety Science, 2012, 50(4): 629−644. DOI: 10.1016/j.ssci.2011.08.065.

[11] SU Guo-shao, SHI Yan-jiong, FENG Xia-ting, JIANG Jian-qing, ZHANG Jie, JIANG Quan. True-triaxial

experimental study of the evolutionary features of the acoustic emissions and sounds of rockburst processes [J]. Rock Mechanics and Rock Engineering, 2018, 51(2): 375−389. DOI: 10.1007/s00603-017-1344-6.

[12] GONG Feng-qiang, WU Chen, LUO Song, YAN Jing-yi. Load-unload response ratio characteristics of rock materials and their application in prediction of rockburst proneness [J]. Bulletin of Engineering Geology and the Environment, 2019, 78(7): 5445−5466. DOI: 10.1007/s10064-019-01474-6.

[13] ZHAO X G , WANG J , CAI M , CHENG C, MA LK, SU R, ZHAO F, LIU D J. Influence of unloading rate on the strainburst characteristics of Beishan granite under true-triaxial unloading conditions [J]. Rock Mechanics and Rock Engineering, 2014, 47(2): 467−483. DOI: 10.1007/s00603-013-0443-2.

[14] GONG Feng-qiang, SI Xue-feng, LI Xi-bing, WANG Shan-yong. Experimental investigation of strain rockburst in circular caverns under deep three-dimensional high-stress conditions [J]. Rock Mechanics and Rock Engineering, 2019, 52(5):1459−1474. DOI: 10.1007/s00603-018-1660-5.

[15] LIU Xi-qi, XIA Yuan-you, LIN Man-qing, BENZERZOUR M. Experimental study of rockburst under true-triaxial gradient loading conditions [J]. Geomechanics and Engineering, 2019, 18(5): 481−492. DOI: 10.12989/gae.2019.18.5.481.

[16] ZHU Guang-an, DOU Lin-ming, WANG Chang-bin, DING Zi-wei, FENG Ze-jie, XUE Fei. Experimental study of rock burst in coal samples under overstress and true-triaxial unloading through passive velocity tomography [J]. Safety Science, 2019, 117: 388−403. DOI: 10.1016/j.ssci.2019.04.012.

[17] LIU Guo-Feng, FENG Xia-Ting, FENG Guang-Liang, CHEN Bing-Rui, CHEN Dong-Fang, DUAN Shu-Qian. A method for dynamic risk assessment and management of rockbursts in drill and blast tunnels [J]. Rock Mechanics and Rock Engineering, 2016, 49(8): 3257−3279. DOI: 10.1007/s00603-016-0949-5.

[18] WANG Yang, HE Man-chao, LIU Dong-qiao, GAO Yu-bing. Rockburst in sandstone containing elliptic holes with varying axial ratios [J]. Advances in Materials Science and Engineering, 2019, 2019: 1−17. DOI: 10.1155/2019/5169618.

[19] LUO Yong, GONG Feng-qiang, LIU Dong-qiao, WANG Shan-yong, SI Xue-feng. Experimental simulation analysis of the process and failure characteristics of spalling in D-shaped tunnels under true-triaxial loading conditions [J]. Tunnelling and Underground Space Technology, 2019, 90: 42−61. DOI: 10.1016/j.tust.2019.04.020.

[20] HU Xiao-chuan, SU Guo-shao, CHEN Guan-yan, MEI Shi-ming, FENG Xia-ting, MEI Guo-xiong, HUANG Xiao-hua. Experiment on rockburst process of borehole and its acoustic emission characteristics [J]. Rock Mechanics and Rock Engineering, 2019, 52(3): 783−802. DOI: 10.1007/s00603-018-1613-z.

[21] RUECK M, RAHNER R, SONE H, DRESEN G. Initiation and propagation of mixed mode fractures in granite and sandstone [J]. Tectonophysics, 2017, 717: 270−283. DOI: 10.1016/j.tecto.2017.08.004.

[22] MORADIAN Z, EINSTEIN H H, BALLIVY G. Detection of cracking levels in brittle rocks by parametric analysis of the acoustic emission signals [J]. Rock Mechanics and Rock Engineering, 2016, 49(3): 785−800. DOI: 10.1007/s00603-015-0775-1.

[23] CHANG S H, LEE C I. Estimation of cracking and damage mechanisms in rock under triaxial compression by moment tensor analysis of acoustic emission [J]. International Journal of Rock Mechanics and Mining Sciences, 2004, 41(7): 1069−1086. DOI: 10.1016/j.ijrmms.2004.04.006.

[24] SU Guo-shao, SHI Yan-jiong, FENG Xia-ting, JIANG Jianqing, ZHANG Jie, JIANG Quan. True-triaxial experimental study of the evolutionary features of the acoustic emissions and sounds of rockburst processes [J]. Rock Mechanics and Rock Engineering, 2018, 51(2): 375−389. DOI: 10.1007/s00603-017-1344-6.

[25] ZHANG Yan, FENG Xia-ting, YANG Cheng-xiang, ZHANG Xi-wei, SHARIFZADEH M, WANG Zhao-feng. Fracturing evolution analysis of Beishan granite under true triaxial compression based on acoustic emission and strain energy [J]. International Journal of Rock Mechanics and Mining Sciences, 2019, 117: 150−161. DOI: 10.1016/j.ijrmms.2019.03.029.

[26] SUN Bing, HOU Shan-shan, XIE Jie-hui, ZENG Sheng. Failure prediction of two types of rocks based on acoustic emission characteristics [J]. Advances in Civil Engineering, 2019, 2019(15): 1−11. DOI: 10.1155/2019/5028489.

[27] SUN Xiao-ming, XU Hui-chen, HE Man-chao, ZHANG Fang. Experimental investigation of the occurrence of rockburst in a rock specimen through infrared thermography and acoustic emission [J]. International Journal of Rock Mechanics and Mining Sciences, 2017, 93: 250−259. DOI: 10.1016/j.ijrmms.2017.02.005.

[28] XIAO Fu-kun, HE Jun, LIU Zhi-jun, SHEN Zhi-liang, LIU Gang. Analysis on warning signs of damage of coal samples with different water contents and relevant damage evolution based on acoustic emission and infrared characterization [J]. Infrared Physics & Technology, 2019, 97: 287−299. DOI: 10.1016/j.infrared.2019.01.007.

[29] WANG Shu-ren, LI De-jian, LI Chun-liu, ZHANG Cheng-guo, ZHANG Yan-bo. Thermal radiation characteristics of stress evolution of a circular tunnel excavation under different confining pressures [J]. Tunnelling and Underground Space Technology, 2018, 78: 76−83. DOI: 10.1016/j.tust.2018.04.021.

[30] LIU Shan-jun, WEI Jia-lei, HUANG Jian-wen, WU Li-xin, ZHANG Yan-bo, TIAN Bao-zhu. Quantitative analysis methods of infrared radiation temperature field variation in rock loading process [J]. Chinese Journal of Rock Mechanics and Engineering, 2015, 34(1): 2968−2976. DOI: 10.13722/j.cnki.jrme.2014.0656. (in Chinese)

[31] DU Kun, TAO Ming, LI Xi-bing, ZHOU Jian. Experimental study of slabbing and rockburst induced by true-triaxial unloading and local dynamic disturbance [J]. Rock Mechanics and Rock Engineering, 2016, 49(9): 3437−3453. DOI: 10.1007/s00603-016-0990-4.

[32] WANG Miao-miao, TAN Cheng-xuan, MENG Jing, YANG Bai-cun, LI Yuan. Crack classification and evolution in anisotropic shale during cyclic loading tests by acoustic emission [J]. Journal of Geophysics and Engineering, 2017, 14(4): 930−938. DOI: 10.1088/1742-2140/aa6f24.

[33] ZHANG Yan-bo, LIU Shan-jun. Thermal radiation temperature field variation of hole rock in loading process [J]. Rock and Soil Mechanics, 2011, 32(4): 1013−1017. DOI: 10.16285/j.rsm.2011.04.003. (in Chinese)

(Edited by HE Yun-bin)

中文导读

含孔花岗岩岩爆破坏过程及时空演化规律实验研究

摘要：为了研究岩爆机理和时空演化规律，采用预制圆孔花岗岩试件进行不同侧向载荷下的岩爆模拟试验，利用微型摄像机、声发射(AE)系统和红外热像仪等监测系统，研究岩爆的声发射特征和热辐射温度运移，此外还分析了围岩的破裂模式及损伤演化。结果表明，侧向载荷的升高对孔洞的承载能力起到先增强后弱化的作用，岩爆可分为平静期、颗粒弹射期、稳定破坏期、全面崩塌期 4 个阶段，声发射信号演化为由平静演变为间断出现，然后，持续发生伴随突增，最终急剧破坏；围岩破坏以拉伸破坏为主，剪切破坏呈现先增多后减少的趋势；颗粒弹射期孔洞损伤逐渐增加，但岩爆的损伤主要集中在稳定破坏期；热辐射温度运移表现为浅部升温，向内扩展，浅部降温，自由面升温，向内扩展，岩爆坑温度骤升，试件破坏。表面支护的初期加固作用应该被充分发挥作用，巷道支护体系应具备适当的抗拉能力和良好的吸能能力。

关键词：岩爆；声发射；时空演化；热成像